Influences of ENSO-Induced Indo–Western Pacific SST Anomalies on Extratropical Atmospheric Variability during the Boreal Summer

NGAR-CHEUNG LAU, ANTS LEETMAA, AND MARY JO NATH

NOAA/Geophysical Fluid Dynamics Laboratory, Princeton University, Princeton, New Jersey

HAI-LAN WANG

Program in Atmospheric and Oceanic Sciences, Princeton University, Princeton, New Jersey

ABSTRACT

The causes for the observed occurrence of anomalous zonally symmetric upper-level pressure ridges in the midlatitude belts of both hemispheres during the year after warm El Niño–Southern Oscillation (ENSO) events have been investigated. Sea surface temperature (SST) anomalies in the Indo–western Pacific (IWP) sector were simulated by allowing an oceanic mixed layer model for that region to interact with local atmospheric changes forced remotely by observed ENSO episodes in the eastern/central tropical Pacific. The spatiotemporal evolution of these SST conditions through a composite ENSO cycle was then inserted as lower boundary conditions within the IWP domain in an ensemble of atmospheric general circulation model (GCM) integrations. This experimental setup is seen to reproduce zonally symmetric geopotential height anomalies with maximum amplitudes being attained over the extratropics in the boreal summer after the peak phase of ENSO. The model evidence hence supports the notion that these global-scale atmospheric changes are primarily responses to SST perturbations in IWP, which are in turn linked to ENSO variability in the equatorial Pacific by the "atmospheric bridge" mechanism.

Experimentation with a stationary wave model indicates that the Eastern Hemisphere portion of the aforementioned atmospheric signals are attributable to forcing by tropical heat sources and sinks associated with precipitation anomalies in the IWP region, which are closely related to the underlying SST changes. Diagnosis of the output from the GCM integrations reveals that these circulation changes due to diabatic heating are accompanied by alterations of the propagation path and intensity of the high-frequency eddies at locations farther downstream. The geopotential tendencies associated with the latter disturbances bear some resemblance to the anomalous height pattern in the Western Hemisphere. Such local eddy–mean flow feedbacks hence contribute to the zonal symmetry of the atmospheric response pattern to forcing in the IWP region. Analysis of zonally averaged circulation statistics indicates that the mean meridional circulation induced by divergence of anomalous transient eddy momentum fluxes in ENSO events could also generate zonally symmetric perturbations in midlatitudes.

The model-simulated precipitation and surface temperature anomalies in the North American sector in response to SST changes in IWP suggest an increased frequency of droughts and heat waves in that region during the summer season after warm ENSO events.

1. Introduction

Changes in the sea surface temperature (SST) conditions over the Indian and western Pacific Oceans during El Niño–Southern Oscillation (ENSO) events in the eastern/central equatorial Pacific have been recognized

Corresponding author address: Ngar-Cheung Lau, NOAA/ Geophysical Fluid Dynamics Laboratory, P.O. Box 308, Princeton, NJ 08542.
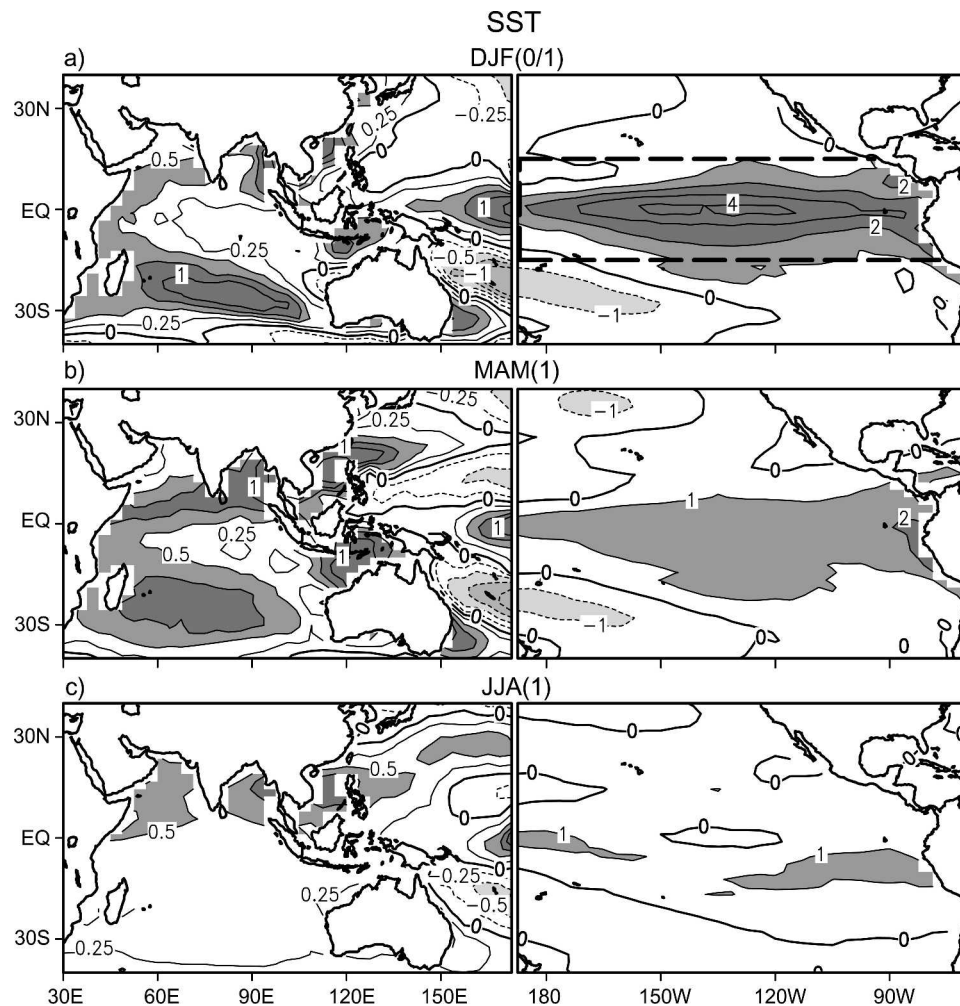E-mail: gabriel.lau@noaa.gov

in many observational studies (e.g., Hsiung and Newell 1983; Pan and Oort 1983, 1990; Kawamura 1994; Lanzante 1996). It has been noted that, whereas the peak phase of the ENSO-related SST signal in the central tropical Pacific occurs in the northern winter, the SST anomalies in the Indo–western Pacific (IWP) sector typically attain maximum amplitudes one to two seasons later, that is, during the following boreal spring or early summer. Recent diagnoses (e.g., Klein et al. 1999) reveal that the SST variations in IWP may partially be attributed to anomalous heat and radiative fluxes

SST

FIG. 1. Distributions of the prescribed SST anomaly in in the deep tropical Pacifc Ocean [DTEP, see thick dashed rectangular border in right panel of (a)]) and model-generated SST anomaly outside of DTEP in the MLM experiment. Results are based on differences between composites over five warm and five cold ENSO events, for the periods of (a) DJF(01), (b) MAM(1), and JJA(1). The year number in parentheses of the time labels refers to the year in the ENSO time frame, with (0) indicating the year when the events initiated, and (1) denoting the following year. Contour intervals: (left) 0.25° and (right) 1°C.

across the local air–sea interface. These surface fluxes are modulated by the overlying atmospheric conditions, such as wind speed, temperature, moisture content, and cloud cover. The latter meteorological changes over the IWP are in turn remotely forced by ENSO anomalies situated in the central tropical Pacific. The SST variability in IWP is hence linked to ENSO through an "atmospheric bridge" spanning the Pacific and Indian Oceans.

The effectiveness of the chain of processes described above in modulating the atmospheric and oceanic conditions in the IWP sector has been demonstrated in a series of general circulation model (GCM) experiments analyzed by Lau and Nath (2003, hereafter LN03). In

that study, observed monthly varying SST anomalies were prescribed as lower boundary conditions in the deep tropical eastern/central Pacific (DTEP), whereas the model atmosphere is coupled to a motionless oceanic mixed layer model outside of this forcing domain. More details of this experimental design will be provided in section 2. The composite distributions of the SST field, as obtained by subtracting the averages over five outstanding cold ENSO events from averages over five strong warm events, are displayed in Fig. 1. Results are presented for the boreal winter (when the imposed ENSO forcing typically attains maximum amplitudes), as well as the following spring and summer of these outstanding episodes. The box with dashed boundary in

the right portion of Fig. 1a indicates the DTEP site. The SST conditions at all grid points beyond this region have been predicted by the oceanic mixed layer model. The patterns in Fig. 1 indicate that the simulated SST changes in the IWP sector are mostly positive during warm ENSO events in the tropical central Pacific. Some of these model features are discernible in the corresponding composites based on observations (see LN03). The development of the SST anomalies in IWP exhibits noticeable temporal lags relative to that in DTEP. The strength of the composite SST forcing in the core of DTEP is seen to diminish from boreal winter (Fig. 1a) to the following spring and summer (Figs. 1b–c). On the contrary, the SST perturbations at most sites in the northern Indian Ocean as well as the marginal seas off the Chinese and northwestern Australian coasts are noticeably enhanced from northern winter to spring. The warm anomalies in IWP north of the equator also tend to persist through the following summer.

The SST anomalies in IWP that are generated by ENSO forcing from the tropical Pacific could in turn exert influences on the atmospheric circulation. We have investigated the nature of these feedback effects by comparing the output from GCM experiments with and without atmosphere–ocean coupling outside of the ENSO forcing region in DTEP, or by subjecting the model atmosphere to SST anomalies in IWP as produced by the atmospheric bridge mechanism. Lau and Nath (2000) and LN03 have reported that the SST increases in the northern Indian Ocean during warm ENSO events lead to substantial changes in the intensity of the monsoonal circulation over South Asia. The evidence presented in Wang et al. (2000), LN03, and N.-C. Lau et al. (2004, hereafter LNW04) also indicates that the SST warming in the South and East China Seas and the cooling in the subtropical Pacific near the date line during warm ENSO episodes (see Fig. 1b) play a prominent role in the evolution of the anomalous surface anticyclone in that region.

In addition to their salient relationships with the local atmospheric environment, the SST changes in IWP may have more widespread impacts on interannual variability in other parts of the globe. For instance, Hoerling et al. (2001b), Kumar et al. (2001), and Hoerling and Kumar (2003) documented the prolonged warmth and dryness of the extratropical belts (particularly North America, southern Europe, and southwestern Asia) after the 1997 El Niño and suggested that these anomalies could be caused by the SST increase in the IWP sector. The probable effects of SST variations in IWP on North Atlantic climate were pointed out by Hoerling et al. (2001a). Kumar and Hoerling (2003) further showed that the continuation of tropicwide tropospheric warm-

ing during the several seasons after the peak phase of El Niño events could result from the delayed temperature increases of the tropical Indian and Atlantic waters. The links between the Asian summer monsoons and the circulation/precipitation over continental North America have been considered by Lau and Weng (2002) and K. M. Lau et al. (2004). In view of the aforementioned influences of SST anomalies in IWP on the intensity of the Asian monsoons, the oceanic conditions in IWP could play an important role in the covariability between summer climates over Asia and North America.

In the present study, a concerted effort is made to examine the impacts of SST variations in IWP on the global atmospheric circulation and to diagnose the dynamical processes that account for the local and remote aspects of these impacts. Our attention is focused on the SST perturbations generated by the atmospheric bridge, so as to demonstrate the far-reaching effects of this mechanism on global atmospheric variability during ENSO events. By building upon the previous modeling studies of LN03 and LNW04, we present results based on a new suite of experiments that are specifically designed to delineate the atmospheric responses to SST changes in IWP.

The model experiments analyzed in this study are documented in section 2. The influences of SST anomalies in IWP on atmospheric conditions in different parts of the globe, as inferred from the model runs, are diagnosed in section 3. The local processes that contribute to these atmospheric signals are examined in section 4. The role of eddy–mean flow interactions in the maintenance of these signals is analyzed using a zonally averaged framework in section 5. Implications of the remote atmospheric responses on the summertime variability of the North American climate are considered in section 6.

2. Designs of model experiments

The basic model tool for this study is an atmospheric GCM maintained by the Climate Dynamics Project at the Geophysical Fluid Dynamics Laboratory. This global model uses a spectral framework with rhomboidal truncation at 30 wavenumbers and has 14 sigma levels in the vertical direction. Documentation of various aspects of this model may be found in Gordon and Stern (1982) and Broccoli and Manabe (1992). A comprehensive set of circulation statistics on the climatology and variability of the GCM has been compiled by Alexander and Scott (1995).

The following four experiments based on the above GCM have been analyzed in the course of this investigation:

a. The mixed layer model (MLM) experiment

Observed monthly varying SST data for the 1950–99 period have been inserted as lower boundary conditions in the DTEP region (15°S–15°N, 172°E to the South American coast; see dashed border in the right portion of Fig. 1a). For maritime sites outside of this region, two-way atmosphere–ocean interactions have been incorporated by coupling the model atmosphere to a static-ocean mixed layer model with variable thickness (see Gaspar 1988; Alexander et al. 2000). This mixed layer model computes SST variations at individual grid points in response to the local atmospheric driving. The flux correction technique described by Manabe et al. (1991) has been applied so as to ensure that the seasonal cycle of the long-term-averaged SST pattern as generated by the mixed layer model is almost identical to the observed climatological distributions. Altogether, 16 parallel integrations over the 50-yr period have been conducted, with each run being initiated from an independent set of atmospheric conditions.

b. The control (CTRL) experiment

Temporally varying SST forcing has been prescribed in DTEP in the same manner as in the mixed layer model (MLM) experiment. However, no air–sea coupling has been performed beyond the DTEP region. Instead, the observed climatological seasonal cycle of the SST field has been imposed on all grid points outside of DTEP; that is, interannual SST variability is absent at these points. An ensemble of eight model runs have been conducted under this scenario.

c. The Indo–western Pacific (IWP) SST experiment

This experiment is aimed at delineating the atmospheric response to SST anomalies in the IWP sector (40°S–40°N, 30°–165°E; i.e., domain of the left portion of Fig. 1) that are linked to ENSO through the atmospheric bridge mechanism. The oceanic boundary forcings used here have been obtained by the following composite procedure. The 16-member ensemble mean SST values generated in the MLM experiment have been averaged over the five outstanding warm ENSO episodes starting in 1957, 1972, 1982, 1991, and 1997. Similarly, averages have been taken over the five cold events starting in 1955, 1970, 1973, 1975, and 1988. These computations have been performed at monthly intervals from January of the year when the events initiated (year 0) to February two years thereafter (year 2). The difference between the two sets of composites (hereafter referred to as "warm minus cold composites") have been multiplied by a factor of 2^{1} and then added to the local climatological value. The evolution of the resulting SST field through the 26-month composite period in the IWP region was then applied as lower boundary conditions. All grid points located outside of IWP, including those in DTEP, were constrained to evolve through the climatological annual cycle as determined by observational data. The 26-month integrations were repeated 30 times by using different atmospheric initial conditions.

d. The climatological SST (CLIMO) experiment

To compute the climatological state of the model atmosphere, from which the anomalous component of various fields of interest in the IWP experiment could be evaluated, a 30-yr experiment has been performed using observed climatological SST conditions at all grid points throughout the world oceans.

It is noteworthy that, through implementation of the flux correction procedure in the MLM experiment, the observed SST climatology prescribed in the control (CTRL) experiment (outside of DTEP), IWP (outside of Indo–western Pacific), and climatological SST (CLIMO) experiment (worldwide) is the same as the long-term means of the SST conditions as computed by the oceanic mixed layer model outside of DTEP in MLM.

The MLM and CTRL experiments described above are identical to those examined in Alexander et al. (2002), LN03, and LNW04, who have provided more details of these model runs. The same pair of experiments have also been examined by Kumar and Hoerling (2003), who have referred to them as the POGA-ML and POGA integrations, respectively.

Most of the results presented in this study are based on ensemble averages over the 16, 8, 30, and 30 samples available in the MLM, CTRL, IWP, and CLIMO experiments, respectively. Throughout the course of this study, we examine the differences between the output from two experiments, or the warm minus cold composite charts based on a given experiment. To assess the statistical significance of the signals appearing in these individual patterns, the Student's t test has been applied to most of the findings presented here. The results of this assessment are summarized in the appendix. A large majority of the features to be discussed in

---

[1] In view of the rather modest amplitudes of the SST signals in the IWP domain (see Fig. 1), this doubling of the SST forcing is aimed at obtaining more robust atmospheric responses. The results from LNW04 and from model runs subjected to SST forcing of reversed sign (not shown) indicate that the amplitude of the simulated atmospheric response exhibits a quasi-linear dependence on the strength and polarity of the prescribed SST forcing in the western Pacific.
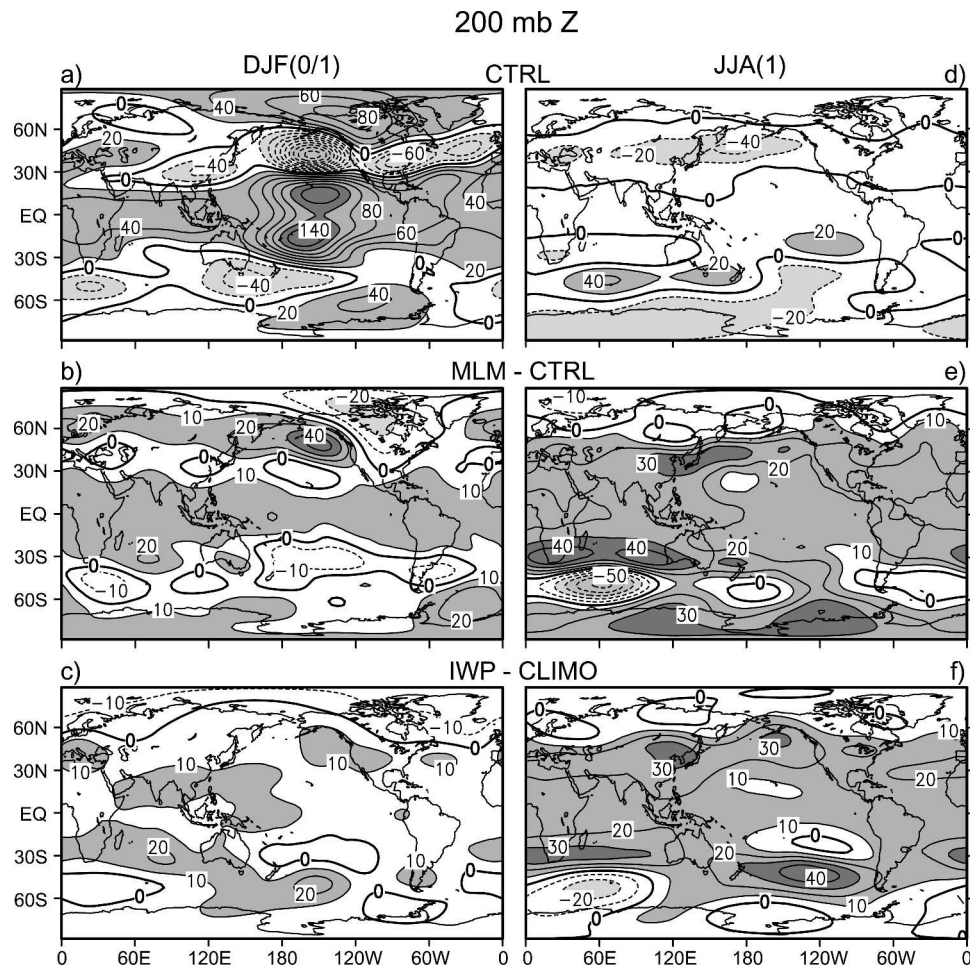
200 mb Z

Fig. 2. Distributions of the 200-mb height anomaly, as obtained from the (a), (d) CTRL experiment, (b), (e) difference between the MLM and CTRL experiments, and (c), (f) difference between the IWP and CLIMO experiments. Results in upper four panels are based on the warm minus cold composites. Data for the (left) DJF(01) and (right) JJA(1) periods. To facilitate comparisons with the other panels in this figure, the anomalies in (c) and (f) are plotted at half amplitude. Contour intervals: (a), (d) 20 and (b), (c), (e), (f) 10 m.

the following sections are seen to exceed the 99% significance level.

3. Global atmospheric changes associated with SST variability in DTEP and IWP

a. Latitude–longitude patterns

The distributions of the 200-mb height anomalies during the DJF(01) and JJA(1) seasons[2] are displayed

---

[2] A certain month or season in the ENSO time frame will hereafter be indicated by using the first three letters of that month or the first letter of the three months in that season, followed by the year indicator (see definitions in section 2) in parentheses. For instance, Jan(0) denotes January of year 0; DJF(01) stands for averages over Dec(0), Jan(1) and Feb(1); JJA(1) represents the June–August season in year 1, etc.

in the left and right panels of Fig. 2, respectively. The top panels show the warm minus cold composites (see definition in section 2) based on output from the CTRL experiment. The patterns in the middle panels are obtained by subtracting the warm minus cold composites based on CTRL data from the corresponding composites produced by the MLM experiment. The differences between the ensemble averages generated in the IWP and CLIMO integrations are presented in the bottom panels. As can be deduced from the designs of the experiments considered here (see details in section 2), the results in the top panels illustrate the typical response of the model atmosphere to the ENSO forcing imposed in the DTEP region. This direct ENSO effect is removed from the output of the MLM experiment while computing the results in the middle panels so that the

signals displayed therein indicate atmospheric perturbations due to air–sea interactions occurring outside the DTEP region. Such interactions are in turn initiated by the atmospheric bridges linking ENSO forcing in DTEP with SST changes in various parts of the world oceans. The bottom panels are aimed at identifying the atmospheric response to SST anomalies in the IWP domain that are generated by the atmospheric bridge mechanism as simulated in the MLM experiment. Recalling that the anomalous SST forcing has been enhanced by a factor of 2 in the IWP experiment, the data in the bottom panels are shown at half amplitude so as to facilitate comparisons with signal strengths given in the other panels for the MLM and CTRL experiments.

During the DJF(0/1) season (i.e., the peak phase of ENSO events), the direct atmospheric response to SST changes in DTEP as simulated in CTRL (Fig. 2a) is characterized by a pair of Pacific subtropical anticyclones straddling the equator and by the familiar wave trains spanning the North Pacific–North American region as well as parts of the southern oceans. Also evident in Fig. 2a is the occurrence of positive height anomalies along the entire equatorial belt and of zonally extended negative anomalies between latitudes 30° and 50° in both hemispheres. The amplitude of the height anomalies is much reduced in the following boreal summer (Fig. 2d), when the SST forcing in DTEP is also much diminished (Fig. 1c). The 200-mb height anomalies in this season are mostly negative along the zonal belt between 30° and 60°N. The overall patterns for both seasons are in good agreement with the corresponding observations (Kumar and Hoerling 2003).

The most prominent features in Fig. 2b are located in the Pacific–North American sector, where the polarities of the height anomalies are opposite to those appearing in Fig. 2a. Hence the feedback effects of the SST anomalies outside of DTEP on the atmospheric circulation in that sector tend to weaken the direct response to ENSO forcing in DTEP during winter. This result is in accord with the findings reported by Alexander et al. (2002), who further noted that this negative interference may partially result from air–sea interactions over the North Pacific. The MLM minus CTRL pattern in the JJA(1) season (Fig. 2e) also exhibits a negative spatial correlation with that produced by the CTRL experiment (Fig. 2d). Particularly noteworthy in Fig. 2e are the elongated positive height anomalies along much of the subtropics in both hemispheres. The magnitude of the extratropical signals in Fig. 2b is typically only 20%–30% of the corresponding extrema shown in Fig. 2a (note different contour intervals used in these panels), thus implying that the direct forcing from DTEP plays a dominant role in determining the

atmospheric response during the peak phase of ENSO. The comparable strengths of the anomalies in Figs. 2d and 2e are indicative of the ascending role of air–sea feedbacks outside of DTEP as the ENSO cycle evolves from the peak phase to the following boreal summer.

The extent to which the features seen in Figs. 2b and 2e may be attributed to ENSO-induced SST forcing from the IWP domain may be assessed by comparing these panels with the anomalies generated in the IWP experiment (Figs. 2c and 2f). During DJF(0/1), the imposed SST changes in the IWP region yield rather weak atmospheric anomalies (see Fig. 2c). The much stronger signals in JJA(1) (Fig. 2f) and their notable spatial resemblance to the pattern in Fig. 2e indicate a prominent role for the SST forcing in IWP during the boreal summer. An outstanding characteristic of the distribution in Fig. 2f is the zonal symmetry of the pronounced positive height anomalies near 30°N and 30°S. The direct response to ENSO forcing in DTEP shows almost no evidence of such subtropical ridges in the JJA(1) season (see Fig. 2d).

The distributions of the deviation from climatology of the 200-mb zonal wind, sea level pressure (SLP), and precipitation fields, as simulated in the IWP experiment in JJA(1), are presented in Figs. 3a–c, respectively. The precipitation signals in the IWP sector (Fig. 3c) exhibit a notable spatial correspondence with the prescribed SST anomalies (Fig. 1c). Analysis of the moisture budget (results not shown) indicates that the positive precipitation changes over the monsoon regions in South Asia are attributable to increased evaporation over the above-normal SST zones in the nearby waters and advection of the resulting moisture anomalies by the climatological monsoon circulation. This effect more than compensates for the opposite precipitation changes associated with the weakened monsoon flow due to reduction of the land–sea contrast in that region. The pattern in Fig. 3c also indicates negative precipitation changes along equatorial Africa as well as over central and eastern North America.

The SLP response (Fig. 3b) in low and middle latitudes is characterized by strong east–west asymmetry, with negative anomalies in the IWP sector and positive anomalies elsewhere. Particularly noteworthy are the opposite pressure changes between the Asian landmass and subtropical North Pacific, as well as between the southern Indian Ocean and South Pacific/South Atlantic. Comparison between the patterns in Figs. 2f and 3b reveals that, within the IWP domain, the polarity of the variations in 200-mb height is mostly opposite to that in SLP, thus indicating the prevalence of a baroclinic vertical structure in that region. Conversely, an in-phase relationship between the 200-mb height and SLP fluc-
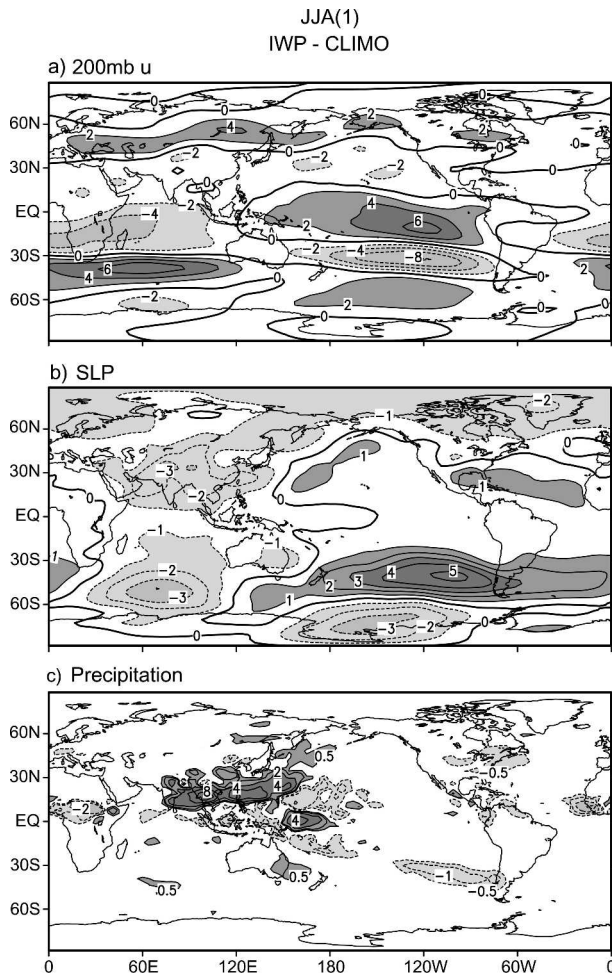
FIG. 3. Distributions of the anomalies of (a) 200-mb zonal wind (u; contour interval: 2 m s^{-1}), (b) SLP (contour interval: 1 mb), and (c) precipitation (contours shown for ± 0.5, ± 1, ± 2, ± 4, and ± 8 mm day^{-1}) as obtained from the difference between the IWP and CLIMO experiments for the JJA(1) season.

tuations is evident over the midlatitude North and South Pacific.

The pattern in Fig. 3a illustrates that easterly (westerly) 200-mb wind anomalies are simulated on the equatorward (poleward) flank of the midlatitude "ridges" in the height field. Comparison between the anomalies in Fig. 3a and the long-term-averaged wind pattern for boreal summer (see Fig. 36 of Alexander and Scott 1995) indicates that these perturbations are associated with poleward displacements of the axes of the climatological jet streams over the North Pacific and the southern oceans.

The counterparts of the panels in Fig. 3 have also been constructed by subtracting the composites based on the CTRL experiment from those based on the MLM experiment. The methodology for computing

such patterns is identical to that used to obtain Fig. 2e for the 200-mb height field. As explained earlier, these MLM–CTRL charts (not shown) may be interpreted as portraying the atmospheric changes generated by two-way atmosphere–ocean coupling outside of the DTEP region; whereas the IWP–CLIMO charts shown in Fig. 3 depict the atmospheric response to SST forcing in the IWP sector. Comparison between these two sets of charts for the wind, SLP, and precipitation fields reveals considerable spatial resemblance between each other in the IWP region. This finding implies that the meteorological signals associated with air–sea feedbacks in the IWP region primarily reflect the response of the atmosphere to SST variations appearing in that site.

b. Zonally averaged patterns

To depict the detailed temporal evolution of the zonally symmetric signals seen in Fig. 2 during the entire ENSO cycle, zonal averages of the monthly mean 200-mb height data from various experiments have been correlated with the Niño-3.4 SST index at various temporal leads and lags. Following the conventional definition, the latter index of ENSO has been constructed by taking the spatial average of the observed SST data within the domain of 5°S–5°N, 120°–170°W for each January of the 1950–99 period. Temporal lag correlation coefficients were then computed between the time series of this index and the zonal means of 200-mb height. The lags considered in this analysis range (in monthly intervals) from −12 months to +13 months. The correlation coefficients thus obtained at various lags and latitude zones are presented in Fig. 4, for height data simulated in the (a) CTRL and (b) MLM experiments. These model results are compared with the corresponding plot based on height data from the observational reanalyses produced by the National Centers for Environmental Prediction–National Center for Atmospheric Research (NCEP–NCAR) for the same 50-yr period (see Kalnay et al. 1996). To facilitate interpretation of the temporal evolution of these correlation statistics in the context of the ENSO time frame, the timing of the Niño-3.4 index is set to be Jan(1). The time labels Jan(0) and Feb(2) denote the correlations as computed with the height data leading Niño-3.4 by 12 months and lagging Niño-3.4 by 13 months, respectively. All correlation values shown in Fig. 4 that exceed the thresholds of ±0.28 and ±0.36 are significant at the 95% and 99% levels, respectively.

As pointed out in many previous studies, the 200-mb height is a good approximation of the local tropospheric thickness and may, hence, be used as a measure
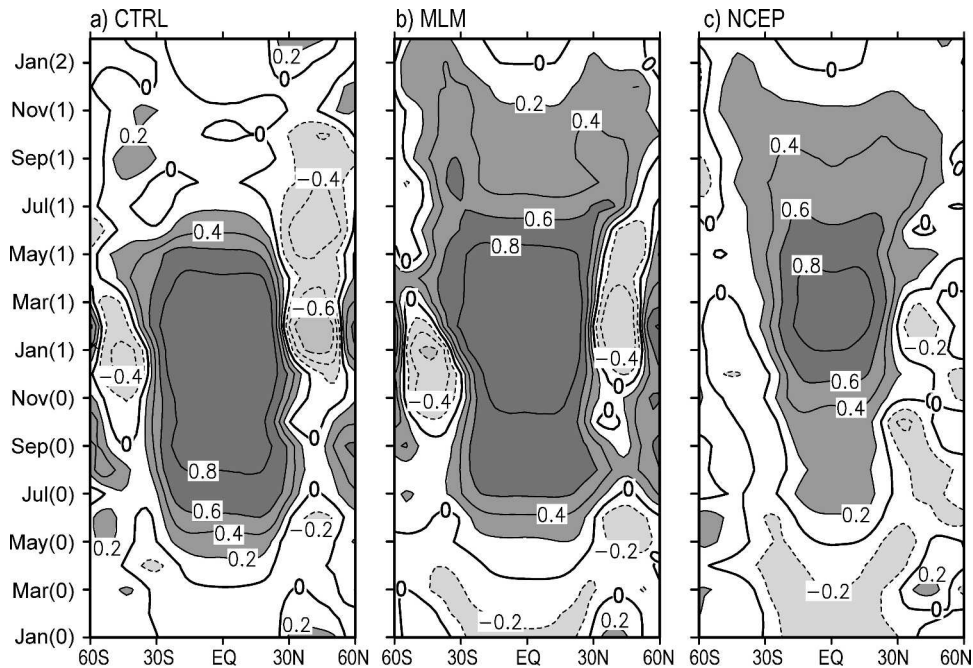
FIG. 4. Correlation coefficients between the Niño-3.4 SST index in Jan and the zonally averaged geopotential height at 200-mb at various temporal leads and lags, based on data from the (a) CTRL and (b) MLM experiments and (c) NCEP–NCAR reanalyses. Results are displayed as functions of time leads and lags (ordinate) and latitude (abscissa). To correspond with the ENSO life cycle, the ordinate axis is labeled using the month and year of the height data used in the computation for a particular time lead or lag. For instance, Jan(1) indicates correlations at zero lag, whereas Jan(0) and Jan(2) indicate correlations with the height data leading and lagging Niño-3.4 by 12 months, respectively. See text for further details. Contour interval: 0.2.

of the mean temperature of the tropospheric column. The statistics based on reanalysis data (Fig. 4c) indicate that the Niño-3.4 index in Jan(1) is most highly correlated with observed tropical 200-mb height 2–3 months later. The positive correlation persists through the northern summer and autumn of year 1. Various observational studies on this temporal development of the tropical tropospheric mean temperature after the peak of ENSO events have been summarized by Kumar and Hoerling (2003). The pattern in Fig. 4c further shows that the tropospheric warming spreads from the equatorial zone toward the northern and southern subtropics during year 1. By the boreal summer and fall of that year, the maximum correlations have shifted to the 30°–40° zone in both hemispheres. A striking example of this phenomenon is the pronounced midlatitude warming after the 1997 El Niño event (Hoerling et al. 2001b; Hoerling and Kumar 2003).

The correlation pattern based on output from the CTRL experiment (Fig. 4a) is characterized by a tropical maximum that attains highest amplitude from autumn of year 0 through spring of year 1. This model result shows little evidence of the observed temporal

lags of warming in the tropical and midlatitude zones in year 1 relative to the Niño-3.4 index, thus illustrating that SST forcing from the DTEP region alone does not account for the delayed atmospheric responses seen in Fig. 4c. Also noteworthy in Fig. 4a are the negative anomalies in the midlatitude zones of both hemispheres. The implied overall tropospheric cooling in the extratropics is discernible from the boreal autumn of year 0 through much of year 1 (see also Figs. 2a and 2d). The observational and model evidence presented by Seager et al. (2003) also indicates extratropical cooling in the JJA(0)–MAM(1) period.

The atmospheric signals generated in the MLM experiment (Fig. 4b) are in much better agreement with the observations. Particularly noteworthy are the forward temporal shift of the near-equatorial correlation maximum in the MLM simulation relative to the CTRL runs and the appearance in the MLM pattern of the two correlation maxima in midlatitudes during the latter half of year 1. The latter signals are indicative of the reversal from extratropical cooling in the earlier part to year 1 to warming thereafter in the MLM experiment. The contrasts between the MLM and CTRL experi-
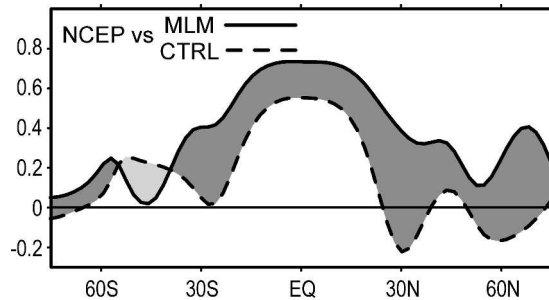
FIG. 5. Distributions of the temporal correlation coefficients between NCEP–NCAR data for zonally averaged 200-mb height and the corresponding ensemble means for the MLM (solid curve) and CTRL (dashed curve) experiments. Computations are based on seasonal averages for JJA in the 1950–99 period.

ments offer further evidence on the central role of SST variability outside of DTEP in tropospheric temperature changes during year 1.

The more realistic simulation of the observed zonal mean height anomalies in the MLM experiment, as compared to that in the CTRL experiment, is further illustrated in Fig. 5. This plot shows the latitudinal distribution of the temporal correlation coefficients between zonally averaged height data from the NCEP–NCAR reanalyses and the corresponding ensemble-mean values in the MLM (solid curve) and CTRL (dashed curve) runs. The computations are based on the 50-yr time series of boreal summer (JJA) means in the 1950–99 period. It is evident from Fig. 5 that, in most latitudes, the height variations in the MLM experiment exhibit a higher correlation with the observations than those in the CTRL experiment.

The actual magnitudes of the simulated height anomalies that contribute to the correlation patterns in Figs. 4a,b can be discerned from the first two panels of Fig. 6, which show the warm minus cold composites of zonally averaged 200-mb height. The results based on the CTRL experiment, and the differences between the MLM and CTRL experiments, are presented in Figs. 6a and 6b, respectively. The format adopted in plotting these panels is identical to that in Fig. 4, that is, the ordinate axis is labeled using the nomenclature outlined in footnote 2. To illustrate the atmospheric changes due to SST anomalies simulated in the IWP sector during the ENSO cycle, the zonal mean 200-mb height anomaly in each month of the Jan(0)–Feb(2) period has been computed by taking the difference between the IWP and CLIMO integrations. The results are displayed in Fig. 6c. To facilitate comparison with the other panels in the same figure, the anomalies shown in Fig. 6c have been reduced by a factor of 2.

The pattern in Fig. 6a indicates that the atmospheric

response to direct SST forcing in DTEP is characterized by a gradual increase in the tropical tropospheric warming from the northern spring of year 0 to winter of year 0/1, and a more abrupt decrease in the warming during the spring of year 1. Also apparent in Fig. 6a are the negative extratropical height anomalies (cooling).

The effects of air–sea interactions induced by the atmospheric bridge mechanism outside of DTEP, as estimated by removing the CTRL signal from the MLM response (see Fig. 6b), are rather weak in year 0 but are relatively much stronger throughout year 1. Near-equatorial warming attains a maximum in the boreal spring and early summer of year 1. In accord with the global chart in Fig. 2e, the zonal mean pattern in Fig. 6b also shows large midlatitude height anomalies in both hemispheres during the northern summer of year 1. The polarity of these extratropical signals tends to be opposite to that simulated in the CTRL experiment during year 1 (Fig. 6a). The overall resemblance between the results in Figs. 6b and 6c implies that the signals seen in the MLM minus CTRL patterns may largely be attributed to the atmospheric response to SST forcing in IWP.

It is worth noting that, during some of the ENSO events used in constructing the warm and cold composites (see lists in section 2), the polarity of the SST forcing in the DTEP region reversed abruptly from year 0 to year 1. For instance, the El Niños of 1972 and 1997 were immediately followed by the La Niñas of 1973 and 1998; whereas the 1975 La Niña occurred prior to the 1976 El Niño. In these particular cases, the observed atmospheric signals in year 1 could result not only from SST forcing in the IWP region (which is induced by the ENSO event in year 0), but also from SST forcing in the DTEP region accompanying an emerging ENSO event (which has a polarity opposite to that of the preceding ENSO event in year 0). The atmospheric impacts of such reversals of ENSO polarity in successive years have been evaluated by examining time–latitude plots similar to Fig. 6a for zonal mean height anomalies simulated by the CTRL experiment in individual events. Inspection of such plots for the 1972/73 and 1997/98 episodes (not shown) reveals that the SST forcing in the DTEP region associated with the warm 1972 and 1997 ENSO events does lead to tropical warming and midlatitude cooling in the latter half of these years and the first several months of the following years. These anomalies are seen to be replaced by tropical cooling and extratropical warming in the latter part of 1973 and 1998, due to occurrence of the cold ENSO events in these years. Analogously, the plot for the 1975/76 period shows a similar sequence of height anomalies but with reversed signs. The corresponding time–latitude
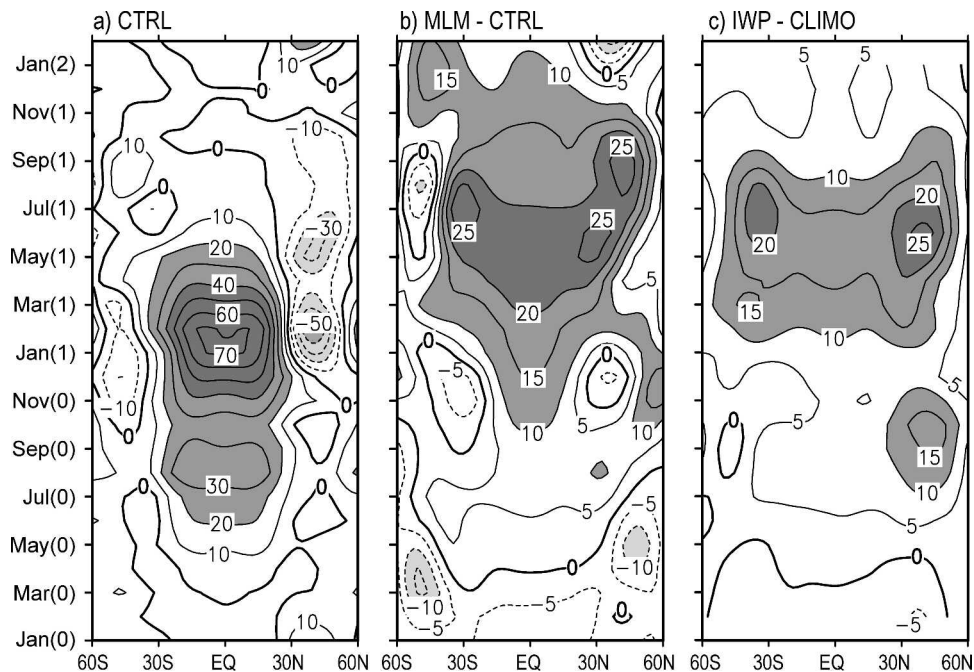
FIG. 6. Warm minus cold composites of the zonally averaged height for the (a) CTRL experiment and (b) difference between the MLM and CTRL experiments. Results are plotted in a similar format as in Fig. 4, with the ordinate axis corresponding to the Jan(0)–Feb(2) period of the ENSO cycle. (c) The temporal evolution of the anomalous zonal mean 200-mb height simulated during the 26-month [Jan(0)–Feb(2)] duration of the IWP experiment, as obtained by subtracting CLIMO data from the IWP output. To facilitate comparison with (a) and (b), the data in (c) have been divided by 2. Contour intervals: (a) 10 and (b), (c) 5 m. A 1:2:1 smoothing in the temporal domain has been applied to the data in (b) and (c).

distributions for the individual cases based on differences between the MLM and CTRL experiments (not shown), which illustrate the effects of air–sea coupling outside of the DTEP region, do however exhibit considerable similarities to the composite pattern in Fig. 6b. In particular, positive midlatitude height anomalies are simulated in the boreal summers of 1973 and 1998, following the El Niños of the preceding years; whereas negative extratropical height anomalies are evident in the year after the 1975 La Niña. In all three events considered here, the amplitude of the midlatitude height anomalies in the MLM minus CTRL panels during the boreal summer of year 1 is comparable to that in the CTRL pattern. Examination of the special cases mentioned above, as well as the other cases incorporated in the composite procedure for constructing Figs. 6a,b, leads us to conclude that the effect of air–sea interactions outside of DTEP on the zonal mean extratropical atmosphere in year 1 is discernible in each of the 10 warm or cold ENSO events selected in this study, irrespective of the transitions in ENSO polarity from year 0 to year 1 during a subset of these events.

4. Local processes contributing to midlatitude atmospheric responses to SST forcing in IWP

a. Role of diabatic heating

The spatial correspondence between the precipitation anomalies in Fig. 3c and the height/pressure anomalies in Figs. 2f and 3b suggests that the simulated atmospheric changes in the vicinity of the IWP region could result from condensational heat sources and sinks due to enhanced and reduced rainfall in that sector. The precipitation pattern is in turn closely related to the SST forcing prescribed in the IWP experiment (see Fig. 1c). To delineate the effects of perturbed diabatic heating on the atmospheric circulation, the three-dimensional, global anomalous heating field as simulated in the IWP experiment has been used to force the stationary wave model (SWM) documented by Ting and Yu (1998). This mechanistic, primitive equation model is time dependent and nonlinear. Its spatial resolution is identical to that of the atmospheric GCM used in this study. The details on the application of this SWM for studying the atmospheric response to prescribed diabatic forcing have been described by LNW04. In the
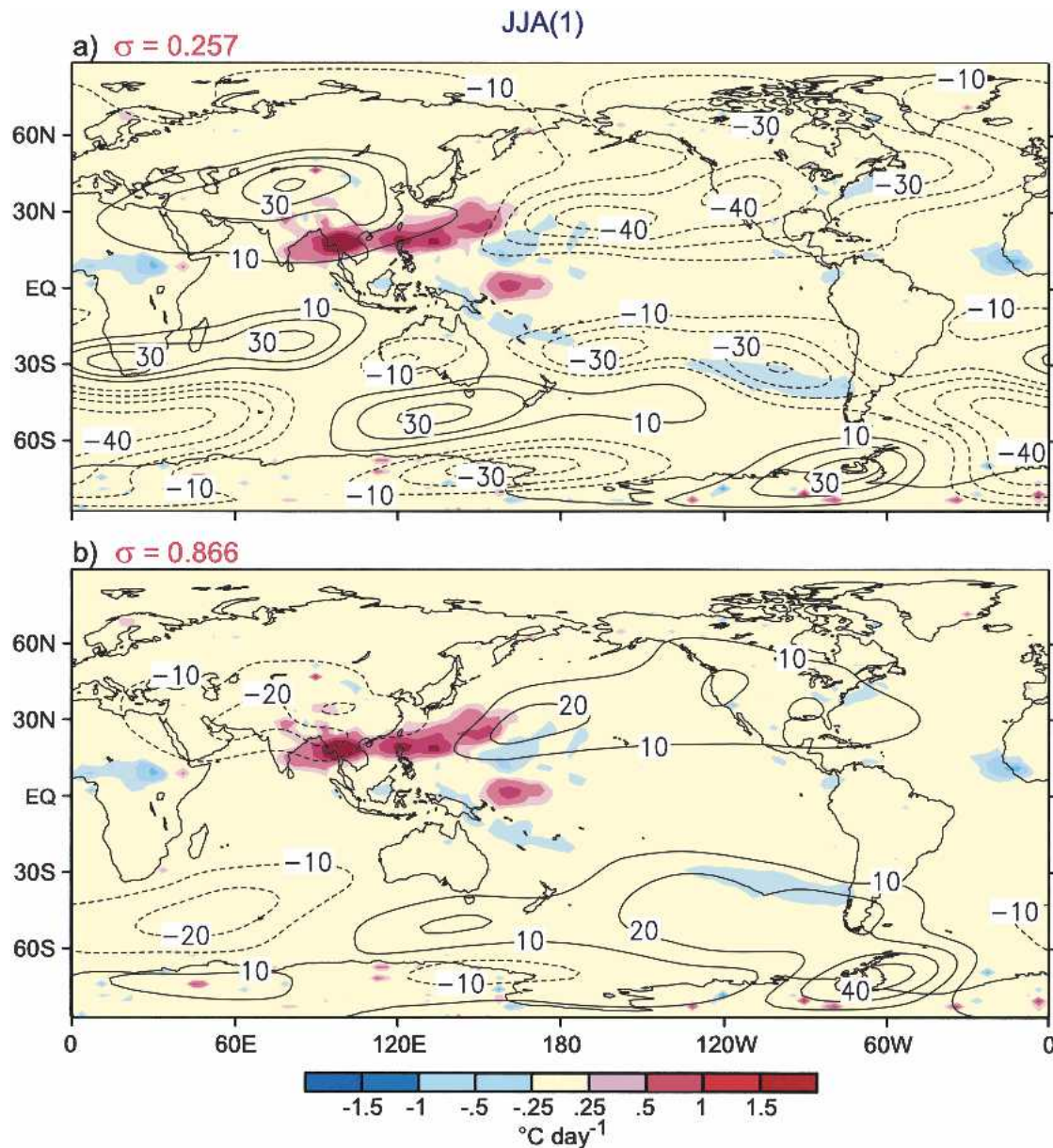
FIG. 7. Distributions of the zonally asymmetric component of the geopotential height response at the (a) 0.257 and (b) 0.866 sigma level to prescribed diabatic heating, as obtained using the stationary wave model for the JJA(1) season. Contour intervals: 10 m. The vertically integrated heating rate used in this computation is indicated by shading.

present computation, the basic state for the SWM has been constructed using the three-dimensional climatology of the atmospheric GCM for the JJA season and has been held fixed through the integration of the SWM. The forcing term for this integration was obtained by subtracting the climatological heating field for northern summer (as generated by the GCM in the CLIMO experiment) from the corresponding field simulated in the IWP experiment during the JJA(1) season. The transient disturbances produced by the SWM were suppressed by strong damping.

The steady-state solution of the SWM in response to the imposed diabatic forcing is portrayed in Fig. 7 using the zonally asymmetric component of the geopotential height field (contours) at the (a) 0.257 and (b) 0.866 sigma levels, which are located in the upper and lower troposphere, respectively, in regions of low terrain. Superposed on these patterns is the distribution of the vertically integrated heating rates (shading) used in forcing the SWM. A separate computation has also been performed by subjecting the SWM to the positive diabatic heating in the Southeast Asian sector (5°–

35°N, 80°–160°E) only. The resulting solution (not shown) bears a strong resemblance to the model response in the Eastern Hemisphere to the global distribution of heat sources and sinks (shown in Fig. 7). This finding indicates that the height patterns in the vicinity of the IWP sector in Fig. 7 are primarily the result of heat sources located in the same region. In comparing Fig. 7a with the GCM results in Fig. 2f, it should be borne in mind that the zonal mean component has a strong presence in the latter pattern; whereas the SWM solution pertains to the departure from the zonal average.

The most prominent heat source in Fig. 7 is located in an elongated zone extending eastward from the Bay of Bengal to the South China and Philippine Seas. This feature bears a strong relationship with the above-normal precipitation field in the same region (Fig. 3c). The low-level response of the SWM to the global distribution of heat sources and sinks (Fig. 7b) consists of negative height anomalies located to the northwest and southwest of the main heating center over Southeast Asia and positive anomalies over the subtropical northwestern Pacific and midlatitude South Pacific. The spatial relationships between these atmospheric features and the heating field are consistent with the analytic solutions for the atmospheric responses to idealized heat sources, as reported by Matsuno (1966) and Gill (1980). The similarity between the pattern in Fig. 7b and the SLP pattern in Fig. 3b indicates that the GCM-simulated features appearing in the latter chart are essentially forced by diabatic processes.
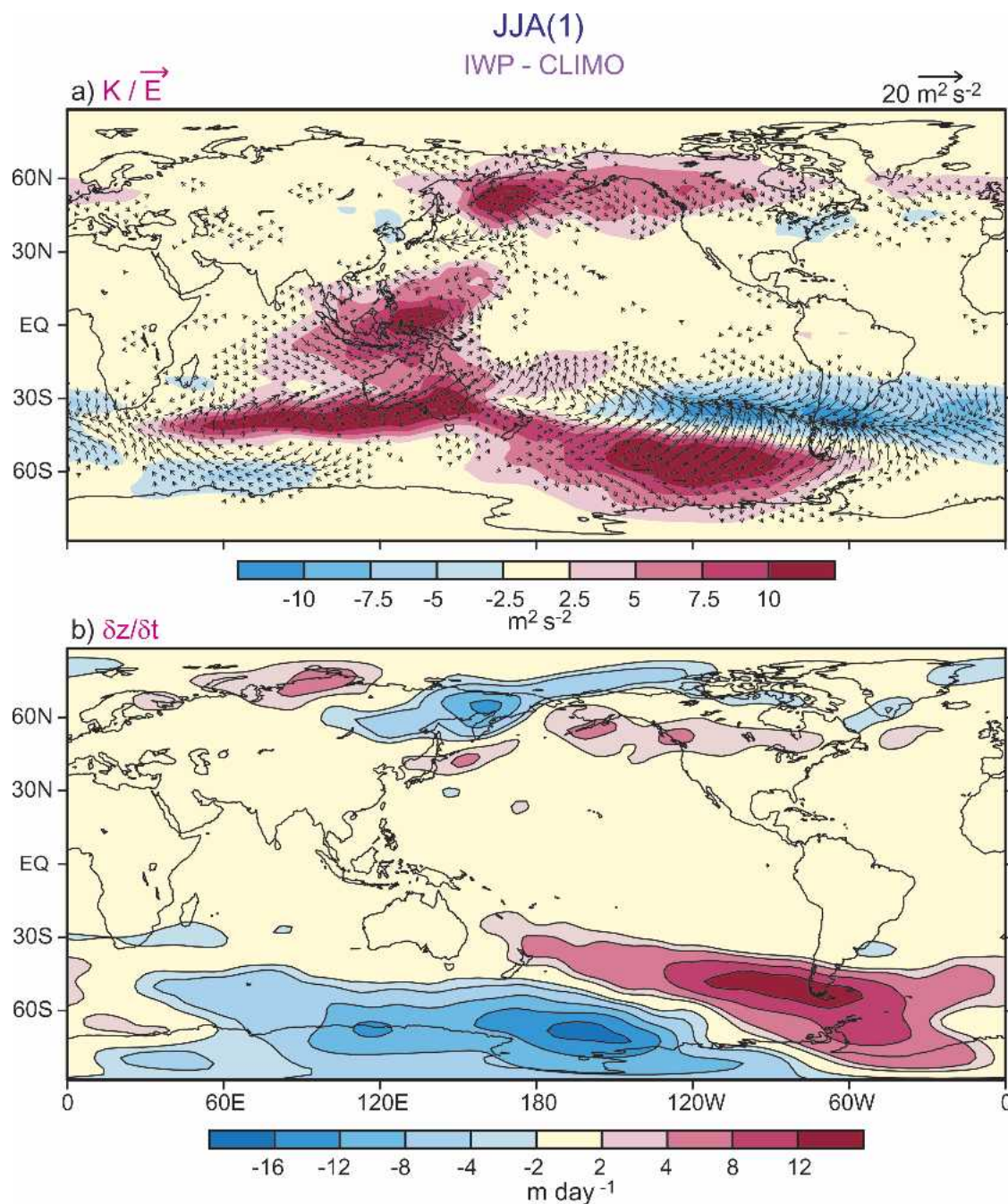
Over much of the tropical and subtropical zones, the polarity of the upper-tropospheric height anomalies in the SWM solution (Fig. 7a) is opposite to that in the lower troposphere (Fig. 7b), thus illustrating the baroclinic nature of these responses. There exists a good correspondence between the signals in Fig. 7a and the 200-mb height anomalies in Fig. 2f within the zone between 0° and 120°E. The pair of midlatitude ridges in the height field across Eurasia and the southern Indian Ocean, as simulated in the IWP experiment (see Fig. 2f), are therefore linked to diabatic forcing. However, the SWM solution deviates markedly from the full GCM result beyond the IWP sector. In particular, there is no evidence in Fig. 7a of the anomalous midlatitude ridges at 200 mb over the North and South Pacific, as seen in the output from the IWP experiment (Fig. 2f).

The recent observational and modeling study by Branstator (2002) has demonstrated that the South Asian jet stream in the boreal winter serves as an effective waveguide for organizing zonally oriented circumglobal patterns with a notable zonal mean component. The role of this mechanism in the generation of

the zonally symmetric patterns, as seen in our present study during the boreal *summer* season, has been evaluated by incorporating the three-dimensional climatological flow structure in JJA in the stationary wave model described in this section. This model was then forced by either idealized subtropical heat sources at various longitudes near the heating centers shown in Fig. 7 or vorticity sources in the vicinity of the North Pacific storm track where enhanced eddy–mean flow feedbacks occur (see section 4b). The geographical extent of the summertime response patterns produced in these experiments (not shown) is much more limited than that generated using the basic state for winter. The weak waveguiding action of the background circulation in JJA may be attributed to the much-reduced intensity of the summertime jet stream in the Northern Hemisphere (see Fig. 36 of Alexander and Scott 1995), and the larger distances separating the heat or vorticity sources from the jet stream core during summer.

b. Role of synoptic-scale transient eddies

We next consider the relationships between extratropical synoptic-scale disturbances and the atmospheric patterns in Figs. 2 and 3. These transient eddies mostly travel eastward along organized storm tracks (e.g., see recent review by Chang et al. 2002). They are modulated by low-frequency changes in the ambient circulation and in turn exert feedback effects on the local background flow pattern as they propagate downstream (e.g., see Lau 1988). To ascertain the role of these synoptic-scale perturbations, the daily 200-mb zonal and meridional wind data (u and v, respectively) from individual samples of the IWP and CLIMO experiments have been subjected to a Lanczos filter (Duchon 1979) that retains time scales between 2 and 10 days. The filtered time series were then used to compute the temporal variance and covariance quantities $\overline{u'u'}$, $\overline{v'v'}$, and $\overline{v'u'}$, where the overbar denotes average over the northern summer and the prime indicates deviation from the seasonal mean. Figure 8 shows the 200-mb distributions of (Fig. 8a) eddy kinetic energy $K = (\overline{u'u'} + \overline{v'v'})/2$ (shading) and extended Eliassen–Palm vector $\boldsymbol{E} = (\overline{v'v'} - \overline{u'u'})/2\boldsymbol{i} - \overline{v'u'}\boldsymbol{j}$ (arrows), and (Fig. 8b) eddy-induced geopotential height tendency $\partial z/\partial t = (f/g)\nabla^{-2}\pi$, where f is the Coriolis parameter, g is the gravitational acceleration, and π is the convergence of eddy vorticity fluxes [which can be evaluated using $\overline{u'u'}$, $\overline{v'v'}$, and $\overline{v'u'}$; see Eq. (2) in Lau 1988]. The results in this figure are obtained by subtracting the climatological eddy statistics for the JJA season in the CLIMO experiment from the corresponding statistics for the JJA(1) season in the IWP experiment. The pattern for K indicates regions of enhanced and diminished synop-

FIG. 8. Distributions of the anomalies of 200-mb (a) transient eddy kinetic energy (*K*; shading) and extended Eliassen–Palm vectors (**E**; arrows; see scale at upper right) and (b) geopotential height tendency induced by transient eddies ($\partial z/\partial t$) as obtained from the difference between the IWP and CLIMO experiments for the JJA(1) season. All computations are based on eddy variance and covariance statistics for time-filtered data with periods of 2–10 days.

tic-scale activity as simulated in the IWP experiment. The **E** vectors are computed using the formulation of Trenberth (1986), who pointed out that the group velocity of the transient eddies relative to the local time mean circulation is parallel to **E** and that the acceleration of the zonal wind due to barotropic eddy processes can be inferred from the divergence of **E**. The eddy-induced height tendency provides a quantitative measure of the barotropic effects of the eddies in forcing the geopotential height pattern.

Comparison between the extratropical patterns for anomalous zonal wind (Fig. 3a) and *K* (Fig. 8a) reveals

that more intense eddy activities develop downstream of positive zonal wind anomalies; whereas weakened transient disturbances are seen to the east of negative changes in the zonal flow. Prominent examples of these relationships include the eastward shift of the maximum in K over Bering Sea–Alaska–northern Canada relative to the enhanced zonal flow over East Asia and the North Pacific; strengthening of storm-track activity along the 30°–40°S zonal belt between 90° and 150°E, which is displaced to the east of the positive zonal wind anomaly over the southern Indian Ocean; and suppression of synoptic-scale variability downstream of the reduced zonal flow over the central South Pacific. Such zonal displacements of the storm tracks in relation to the time-mean circulation have been well documented in many observational and model works (e.g., Blackmon et al. 1977; Frederiksen 1983). These studies demonstrated that the unstable shear regions in the vicinity of strong zonal flows in the extratropics favor the development of synoptic-scale waves, which propagate eastward and attain maximum amplitudes downstream of the unstable sites. Comparison of the anomaly pattern of K in the Western Hemisphere (shading in Fig. 8a) with the corresponding climatological distribution of K (see Fig. 103 of Alexander and Scott 1995) indicates considerable poleward shifts of the storm tracks over the Pacific and Atlantic basin in both hemispheres.

The **E** arrows (Fig. 8a) are predominantly directed eastward near the axes of maximum in K, thus implying enhanced eastward group propagation of the transient eddies relative to the mean flow. In the eastern portion of the elongated maxima in K (i.e., Alaska–northern Canada and east of Australia), the **E** vectors exhibit a distinct divergent pattern, thus indicating acceleration of the zonal flow by the synoptic disturbances in those sites. This feedback effect of the transient eddies on the mean circulation is most discernible toward the eastern end of the enhanced storm tracks, where the synoptic waves typically enter a decay stage dominated by barotropic transfer of kinetic energy to the mean flow through momentum fluxes (e.g., Simmons and Hoskins 1978; Hoskins et al. 1983). The zonal wind acceleration by the transient disturbances would result in an eastward extension of the positive zonal wind anomalies that activate these eddy life cycles in locations farther upstream, thereby enhancing the zonal symmetry of the circulation anomaly. The above relationships are also seen to apply, albeit with opposite polarity, to the belt of suppressed synoptic variability along 30°S in the Western Hemisphere, where the zonal wind deceleration associated with the convergent **E** vectors acts to extend the negative zonal wind anomaly over central South Pacific at 30°S (see Fig. 3a) farther eastward.

Based on geostrophic considerations, the height tendency pattern in Fig. 8b is consistent with the eddy-induced zonal wind changes inferred from the **E** vectors. The regions at and to the east of the maxima in K are straddled by positive (negative) height anomalies on the equatorward (poleward) side so that eastward zonal wind acceleration prevails along the axes of maximum in K. Comparison between the height anomaly simulated in the IWP experiment (Fig. 2f) and the eddy-induced height tendency (Fig. 8b) reveal some spatial correspondence between the two fields in the Western Hemisphere. Of particular note is the coincidence of positive height anomalies with positive height tendencies over the Gulf of Alaska–southern Canada and South Pacific at about 45°S. The time scale for the reinforcement of the extratropical geopotential height field east of the date line by the transient eddies, as estimated by the ratio of the height anomalies[3] to the local height tendency, is approximately 10–20 days. The equivalent barotropic structure of the maritime height/ pressure anomalies in the Western Hemisphere (note in-phase relationships between the features in Figs. 2f and 3b) is indicative of an active role of eddy momentum transports in maintaining these anomalies. An analogous set of relationships between the seasonally averaged circulation pattern, sites of active synoptic-scale disturbances, and eddy-induced height tendency over the North Pacific during the summer of year 0 has been identified by Alexander et al. (2004) using NCEP–NCAR reanalysis data.

5. Zonal mean perspective of the influences of SST variability in DTEP and IWP on eddy–mean flow interactions

The recent diagnostic and modeling study by Seager et al. (2003) has illustrated that modification of the zonal mean subtropical atmospheric structure during ENSO events could alter the distribution of zonal mean momentum transports by these eddies. These authors noted that the resulting changes in the eddy-driven mean meridional circulation could then lead to variations with strong zonal symmetry. To evaluate the role of this mechanism in the zonally averaged responses shown in Fig. 6 for the various GCM experiments examined in this study, the time–space evolution of the relevant zonal mean quantities has been analyzed using output from these model runs. The variation with time

_____

[3] Recalling that the height anomalies are displayed at half amplitude in Fig. 2f, the data presented therein need to be multiplied by a factor of 2 in this estimation.

and longitude of the warm minus cold composites of the 200-mb zonally averaged zonal wind $[u]$, as computed using data from the CTRL experiment, is displayed in Fig. 9a. The corresponding patterns for the zonally averaged 200-mb transient eddy momentum flux $[\overline{v'u'}]$ and its meridional divergence divMF = $\partial([\overline{v'u'}]\cos^2\phi)/a\cos^2\phi\partial\phi$ are presented in Fig. 9c using shading and contours, respectively. The distribution of divMF is repeated in Fig. 9e and is superposed on 500-mb zonal mean pressure velocity $[\omega]$, which is indicated by shading. Here the square brackets denote the zonal averaging operator, a the earth radius, and ϕ the latitude. The analogous results based on departure of the zonal mean statistics of the IWP experiment from the CLIMO experiment are shown in the lower row of panels in Fig. 9. All patterns in Fig. 9 are based on monthly means, with the primes in the covariance quantity $\overline{v'u'}$ representing transient fluctuations from the monthly mean, and the overbar indicating the monthly mean.

The response of $[u]$ to ENSO-related SST forcing in the DTEP region, as produced in the CTRL experiment (see Fig. 9a), is characterized by intensification of the subtropical jets at 20°–30°N and 20°–30°S during the latter half of year 0 and beginning of year 1 of the warm events. These circulation changes are consistent with the enhanced height (and temperature) gradients along the poleward flanks of the positive tropical height anomaly occurring in the mature phase of ENSO (see Fig. 6a). As demonstrated in Seager et al. (2003), the modifications of the meridional potential vorticity gradient of the zonal flow alter the refractive characteristics of the atmospheric basic state, which affect the propagation paths and transport properties of transient disturbances. The changes in eddy momentum fluxes $[\overline{v'u'}]$ are shown in the shading pattern in Fig. 9c. It is seen that strengthening of $[u]$ in the subtropics is concurrent with increased poleward $[\overline{v'u'}]$ in the same latitude zone of both hemispheres and by increased equatorward fluxes near 40°N and 50°S. This configuration of eddy transports is accompanied by notable momentum flux convergences (i.e., divMF < 0) within the ~30°–45° latitude belts in the Northern and Southern Hemispheres (see contours in Fig. 9c). By considering the zonally averaged momentum equation, the divMF term is primarily balanced by the Coriolis torque associated with the zonal mean meridional flow $f[v]$ [e.g., see Eq. (3) of Seager et al. (2003)]. Hence divMF < 0 would be coincident with equatorward $[v]$, and vice versa. Continuity constraints [e.g., Eq. (5) of Seager et al. (2003)] require that meridional convergence and divergence of $[v]$ at the 200-mb level be associated with midtropospheric subsidence ($[\omega] > 0$) and ascent ($[\omega] < 0$), respectively.

The relationship between $[\omega]$ and divMF based on the above reasoning is confirmed by the patterns in Fig. 9e. Since divMF is generally weak in the deep tropical zone (see Fig. 9c), the data values of this quantity and of $[\omega]$ are shown only for latitudes poleward of 25° in Fig. 9e so as to highlight the eddy–mean flow interactions in the extratropics. Of particular interest in the pattern of $[\omega]$ in Fig. 9e is the prevalence of anomalous rising motion within the ~30°–45° latitude zones in both hemispheres. This ascent attains maximum intensity in DJF(0/1). Eddy momentum flux convergence (divMF < 0, which implies equatorward $[v]$) is situated just equatorward of the sites of anomalous ascent; whereas flux divergence (divMF > 0 and poleward $[v]$) is seen immediately poleward of the same sites. Comparison of the pattern of $[\omega]$ in Fig. 9e with that of zonal mean height in Fig. 6a reveals that the negative height anomalies (cooling) in the extratropical zones near the end of year 0 and the first several months of year 1 are almost collocated with anomalous rising motion in the CTRL experiment. In light of the evidence presented herein, the decrease in midlatitude temperature during late year 0 and early year 1 of warm ENSO episodes is partially attributable to adiabatic cooling accompanying the anomalous ascending motion induced by changes in the transient eddy momentum transports in the extratropics, which are in turn modulated by responses of the zonal mean atmospheric circulation to the SST forcing in the DTEP region. Our findings lend support to the mechanism proposed by Seager et al. (2003) for the occurrence of zonally and hemispherically symmetric modes of atmospheric variability.

The nature of eddy–mean flow interactions in response to SST perturbation in the IWP region is delineated by a parallel set of zonal mean diagnoses based on departures of the output of the IWP experiment from climatology, as shown in the lower panels of Fig. 9. The most prominent changes in the zonal mean wind profile (Fig. 9b) occur in the Mar(1)–Sep(1) period, with weakened zonal flows near 30°N and 30°S and intensified flows farther poleward. These anomalies in $[u]$ reflect the poleward shifts of the jet streams in both hemispheres, as noted earlier in Fig. 3a. Comparison between the patterns of Figs. 9a and 9b indicates that, for a given latitude zone, the $[u]$ anomaly in the IWP experiment is opposite to that occurring in CTRL several months earlier. The patterns of $[\overline{v'u'}]$ and divMF for the IWP experiment (Fig. 9d) show enhanced poleward momentum transports near 50°N and 50°S in the middle of year 1, thus leading to meridional flux divergence (convergence) equatorward (poleward) of these latitudes. The relationships between $[\overline{v'u'}]$ and $[u]$ in IWP (Figs. 9b and 9d) are analogous to those in
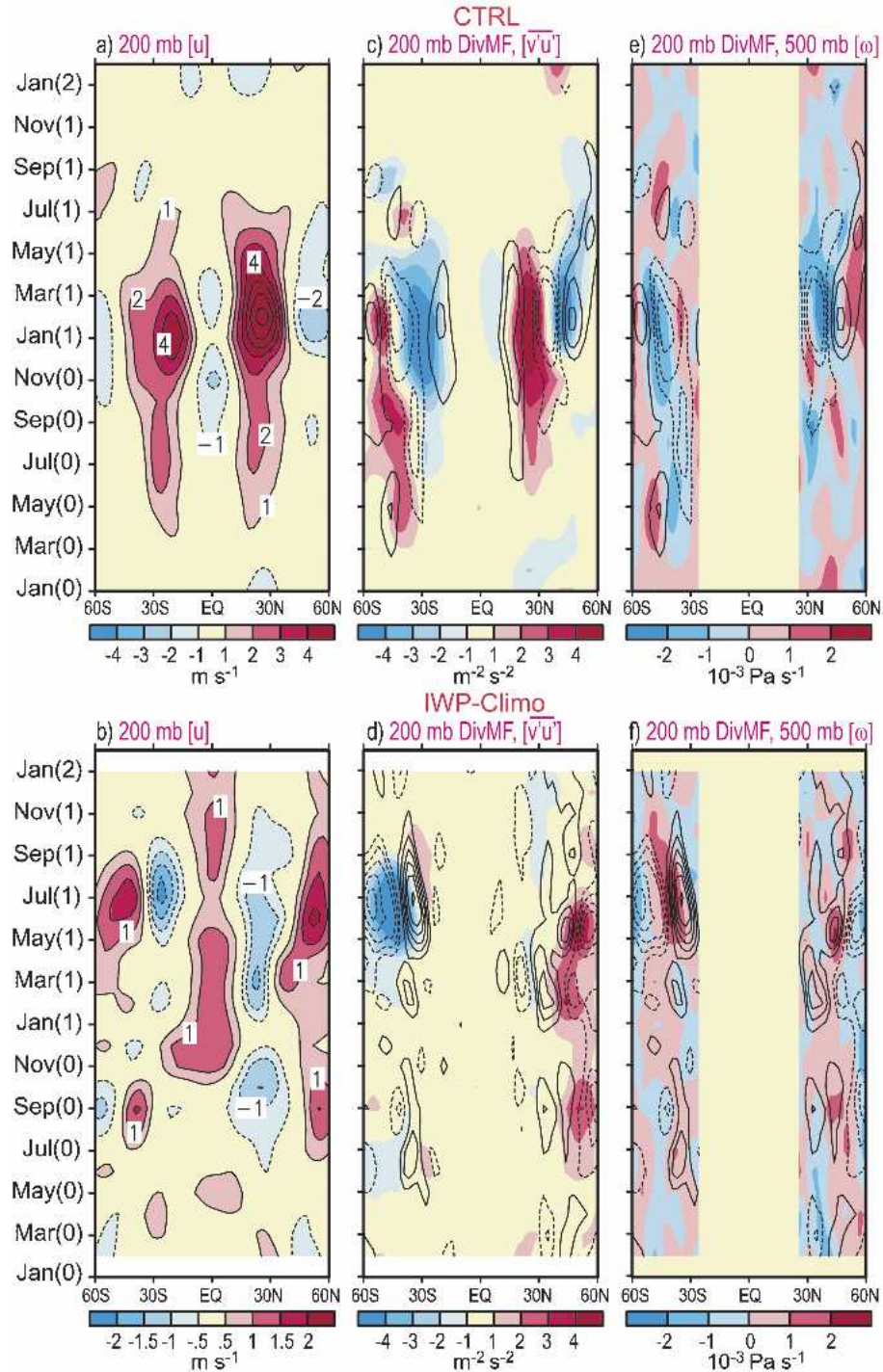
FIG. 9. Distributions of warm minus cold composites of (a), (b) zonally averaged 200-mb zonal wind {[u]; contour intervals: (a) 1 and (b) 0.5 m s^{-1}}, (c), (d) 200-mb zonally averaged transient eddy momentum flux ([$\overline{v'u'}$]; shading) and its meridional divergence [divMF; contours, intervals: (c) 2×10^{-6} and (d) 1×10^{-6} m s^{-2}; solid (dashed) contours indicate positive (negative) values; zero contour not plotted], and (e), (f) eddy momentum flux divergence [divMF; contours, as in (c) and (d)] and 500-mb zonally averaged pressure velocity ([ω]; shading). (a), (c), and (e) are based on data from the CTRL experiment, while (b), (d), and (f) are based on differences between the IWP and CLIMO experiments. All results are displayed as a function of time (ordinate) and latitude (abscissa). A 1:2:1 smoothing in the temporal domain has been applied to the data in all panels. No data are shown equatorward of 25° latitude in (e) and (f).

CTRL (Figs. 9a and 9c), thus suggesting that similar physical interpretations may be applied to the covariability of zonal mean flow structure and eddy transports in both experiments. The patterns of divMF (primarily balanced by $f[v]$) and $[\omega]$ (see Fig. 9f) are seen to satisfy continuity requirements. The most noteworthy signals in the anomalous $[\omega]$ field generated in the IWP experiment are the subsidence near 45° in both hemispheres during the boreal summer of year 1. The timing and location of these features correspond closely with that of the anomalous midlatitude ridges (warming) shown in Fig. 6c. Hence, in analogy with the diagnosis of the CTRL experiment, the lower panels of Fig. 9 illustrate that the zonal mean atmospheric response to SST anomalies in the IWP sector is also linked to adiabatic warming associated with the circulation cells on the meridional plane, which are driven by anomalous eddy transports resulting from changes in the structure of $[u]$.

In summary, the analysis presented in this section offers the following perspective of the zonally symmetric responses of the extratropical atmosphere in the course of a typical warm ENSO cycle. The midlatitude cooling prior to the boreal spring of year 1 is linked to ascending motion induced by transient eddies, whose propagation and transport properties are altered by changes in the mean flow structure due to SST forcing in the DTEP sector. Conversely, the extratropical warming in middle and late year 1 is associated with eddy-driven subsidence, with the eddies being influenced by mean flow anomalies related to SST changes appearing in the IWP region after the peak phase of ENSO. The above sequence of zonal mean changes in the temperature field (as inferred from 200-mb height anomalies) is clearly discernible from the output of the MLM experiment (see Fig. 4b), which incorporates SST forcings from both the DTEP and IWP domains.

6. Impact of circulation changes during JJA (1) on meteorological conditions over North America

The SLP and precipitation charts in Figs. 3b, c suggest that the circulation anomalies examined in the previous sections could exert considerable influences on North American climate during the JJA(1) season. The anomalous patterns of various meteorological fields over North America are shown in greater detail in Figs. 10, for (a) 500-mb geopotential height (contours) and wind vector (arrows) and 1000–500-mb thickness (shading); (b) SLP (contours) and precipitation (shading); and (c) surface wind vector (arrows) and surface air temperature (shading). All results are based on departure from model climatology (as produced by the CLIMO runs) of the fields simulated in the IWP experiment in JJA(1).

The most prominent features in the precipitation and surface air temperature fields (shading in Figs. 10b and 10c) are the dry and warm anomalies extending eastward from the northern plains of the United States across the Great Lakes region to southeastern Canada and the northeastern United States. Below-normal SLP prevails over these anomalies, and a surface cyclonic center is discernible east of the Rockies at ~40°N. The surface circulation south of the principal warm/dry anomaly is characterized by intensified southerly/southwesterly flows (Fig. 10c) with attendant positive temperature advection. A high SLP anomaly, accompanied by anticyclonic circulation, is seen over the southeastern United States and the Gulf Coast. In the middle troposphere (Fig. 10a), a strong positive height and 1000–500-mb thickness anomaly with a distinct anticyclonic flow pattern is seen above the warm/dry zone. Much-below-normal soil moisture (patterns not shown) is also simulated in this zone in the summer season, as well as in the preceding spring and winter [MAM(1) and DJF(0/1)]. Such concurrent and precursory signals are suggestive of a role for ground hydrology in the maintenance and initiation of the warm/dry episodes.

The local relationships between summertime anomalies over North America in different meteorological variables, as deduced from the model results presented in Fig. 10, are in broad agreement with those observed during heat waves and droughts in the U.S. Great Plains, as documented by Klein (1952), Namias (1955), and Chang and Wallace (1987).

The simulated precipitation and surface temperature signals seen in Fig. 10 have been compared with the anomalies observed in the individual summers included in these composites. The observational precipitation datasets examined here include the station records compiled by Dai et al. (1997), as well as the products of the Global Precipitation Climatology Project (GPCP) (see Huffman et al. 1997), which combine rain gauge and satellite measurements with model estimates. Information on the observed surface air temperature is obtained from the NCEP–NCAR reanalyses. Of the five warm ENSO events examined in this study, the observations (not shown) indicate that the summers of 1973, 1983, and 1998 [which correspond to year 1 of the 1972, 1982, and 1997 El Niños] are characterized by below-normal precipitation and above-normal temperature over portions of North America. Conversely, positive precipitation anomalies are observed in the summers of 1971, 1974, and 1989, following the La
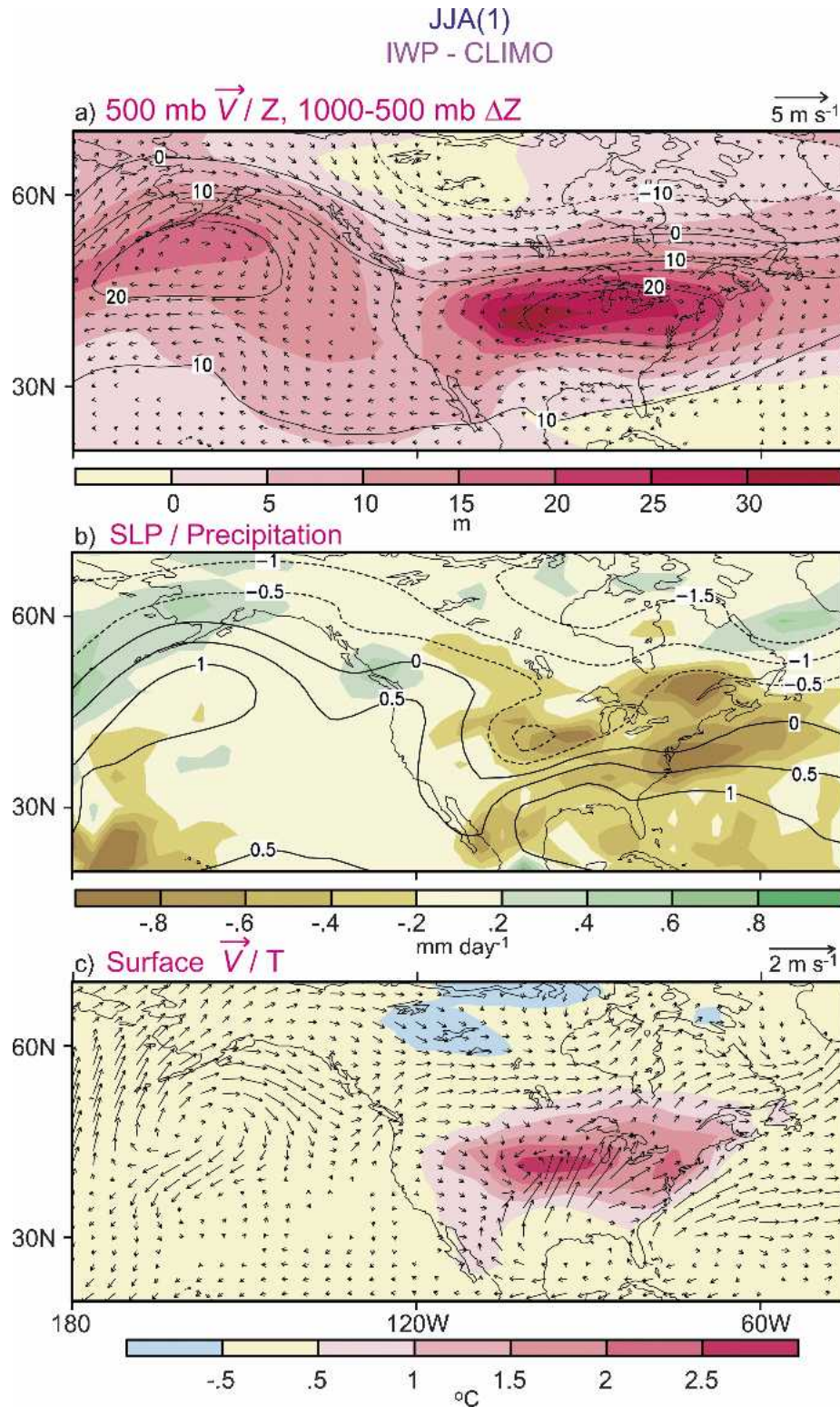
JJA(1)
IWP - CLIMO

a) 500 mb $\vec{V}$ / Z, 1000-500 mb ΔZ $\overset{\longrightarrow}{5\ m\ s^{-1}}$

b) SLP / Precipitation

c) Surface $\vec{V}$ / T $\overset{\longrightarrow}{2\ m\ s^{-1}}$

FIG. 10. Distributions in the North Pacific–North American sector of the anomalies of (a) 500-mb wind vector (**V**; arrows; see scale at upper right) and height (*z*; contours, interval: 10 m) and 1000–500-mb thickness (Δ*z*; shading); (b) SLP (contours, interval: 0.5 mb) and precipitation (shading); and (c) surface wind vector (**V**; arrows; see scale at upper right) and surface air temperature (*T*; shading), as obtained from the difference between the IWP and CLIMO experiments for the JJA(1) season.

Niñas of the preceding years. The agreement between the anomaly patterns simulated in the IWP experiment and the observations in individual ENSO episodes is generally rather weak. Such discrepancies between model and observations could result from limited sampling of the observed anomaly (only one realization for each event), impact of the atmospheric and hydrological conditions prior to the summer of year 1, and additional effects on the observed climate system due to SST anomalies situated outside of the IWP region, as well as various model deficiencies.

7. Summary

An effort has been made to identify the physical causes for the occurrence of midlatitude warming and upper-level pressure ridges with distinct zonal symmetry in the year after El Niño events. Simulated SST anomalies in the IWP region, as produced by the atmospheric bridge mechanism linking ENSO events in the tropical Pacific to that sector, have been used to force an atmospheric GCM through an ENSO life cycle. This experimental setup has considerable success in reproducing the essential characteristics of the atmospheric changes observed after the mature phase of ENSO, thus signifying that the ENSO-induced SST variability in IWP exerts a strong influence on the global atmospheric circulation in year 1.

As deduced from supplementary experiments using a mechanistic stationary wave model and from further diagnosis of the output from the IWP runs, the positive geopotential height anomalies over Eurasia and the southern Indian Ocean are seen to be responses to condensational heating associated with increased precipitation near the abnormally warm waters in the Bay of Bengal as well as the South China and Philippine Seas. More vigorous feedbacks between the synoptic-scale transient disturbances and the local quasi-stationary flow occur downstream of these responses to diabatic heating. Such eddy–mean flow coupling is strongest in the Western Hemisphere and is accompanied by eastward extension of the midlatitude ridges to the North Pacific–North American and South Pacific–South Atlantic sectors. The local manifestation of the above circulation changes over North America is reminiscent of the conditions observed during pronounced summertime heat waves and droughts in that region.

Analysis of the zonally averaged circulation statistics reveals that changes in the extratropical zonal mean geopotential height and temperature in various stages of the ENSO cycle are related to anomalous meridional cells driven by transient eddies, whose propagation and transport properties are modulated by the zonal mean

TABLE A1. Approximate threshold values at the 99% significance level for various fields displayed in different figures of this article.

Figure	Variable	Threshold
1 (left portion)	SST	0.25°C
2	$z_{200\text{ mb}}$	10 m (Tropics)
		20 m (extratropics)
3a	$u_{200\text{ mb}}$	2 m s^{-1}
3b	SLP	1 mb (north of 50°S)
		2 mb (south of 50°S)
3c	Precipitation	0.5 mm day^{-1}
6a, 6b	$z_{200\text{ mb}}$	10 m (Tropics)
		20 m (extratropics)
6c	$z_{200\text{ mb}}$	10 m (all latitudes)
8a	$K_{200\text{ mb}}$	4 m^2 s^{-2}
8b	$\partial z/\partial t$ at 200 mb	2 m day^{-1} (low latitudes)
		4 m day^{-1} (middle latitudes)
		6 m day^{-1} (high latitudes)
10a	$z_{500\text{ mb}}$	10 m (middle latitudes)
		20 m (high latitudes)
	1000–500-mb thickness	10 m
10b	SLP	1 mb
	precipitation	0.5 mm day^{-1}
10c	Temperature	0.5°C

wind structure, which is in turn altered by SST anomalies in the Tropics and subtropics during ENSO.

APPENDIX

Summary of Significance Testing

Most of the fields presented in Figs. 1, 2, 3, 6, 8, and 10 have been subjected to two-tailed Student's *t* tests (Chervin and Schneider 1976), with due consideration of the number of data samples used in constructing the patterns in these individual figures. The approximate threshold values at the 99% significance level for various fields in these figures are given in Table A1. The significance of a given signal in any figure can be assessed by comparing its amplitude with the thresholds given in this table. Those fields with thresholds that exhibit a strong latitudinal dependence are indicated by multiple entries.

REFERENCES

Alexander, M. A., and J. D. Scott, 1995: *Atlas of Climatology and Variability in the GFDL R30S14 GCM.* CIRES, University of Colorado, 121 pp. [Available from the authors at CDC/NOAA, R/E/CD1, 325 Broadway, Boulder, CO 80303-3328.]

——, C. Deser, and J. D. Scott, 2000: Processes that influence sea surface temperature and ocean mixed layer depth variability in a coupled model. *J. Geophys. Res.,* **105,** 16 823–16 842.

——, I. Bladé, M. Newman, J. R. Lanzante, N.-C. Lau, and J. D. Scott, 2002: The atmospheric bridge: The influence of ENSO teleconnections on air–sea interaction over the global oceans. *J. Climate,* **15,** 2205–2231.

——, N.-C. Lau, and J. D. Scott, 2004: Broadening the atmospheric bridge paradigm: ENSO teleconnections to the tropical West Pacific-Indian Oceans over the seasonal cycle and to the North Pacific in summer. *Earth's Climate: The Ocean–Atmosphere Interactions, Geophys. Monogr.,* No. 147, Amer. Geophys. Union, 85–103.

Blackmon, M. L., J. M. Wallace, N.-C. Lau, and S. L. Mullen, 1977: An observational study of the Northern Hemisphere wintertime circulation. *J. Atmos. Sci.,* **34,** 1040–1053.

Branstator, G., 2002: Circumglobal teleconnections, the jet stream waveguide, and the North Atlantic Oscillation. *J. Climate,* **15,** 1893–1910.

Broccoli, A. J., and S. Manabe, 1992: The effects of orography on midlatitude Northern Hemisphere dry climates. *J. Climate,* **5,** 1181–1201.

Chang, E. K. M., S. Lee, and K. L. Swanson, 2002: Storm track dynamics. *J. Climate,* **15,** 2163–2183.

Chang, F.-C., and J. M. Wallace, 1987: Meteorological conditions during heat waves and droughts in the United States Great Plains. *Mon. Wea. Rev.,* **115,** 1253–1269.

Chervin, R. M., and S. H. Schneider, 1976: On determining the significance of climate experiments with general circulation models. *J. Atmos. Sci.,* **33,** 405–412.

Dai, A., I. Fung, and A. D. Del Genio, 1997: Surface observed global land precipitation variation during 1900–88. *J. Climate,* **10,** 2943–2962.

Duchon, C., 1979: Lanczos filtering in one and two dimensions. *J. Appl. Meteor.,* **18,** 1016–1022.

Frederiksen, J. S., 1983: Disturbances and eddy fluxes in Northern Hemisphere flows: Instability of three-dimensional January and July flows. *J. Atmos. Sci.,* **40,** 836–855.

Gaspar, P., 1988: Modeling the seasonal cycle of the upper ocean. *J. Phys. Oceanogr.,* **18,** 161–180.

Gill, A. E., 1980: Some simple solutions for heat-induced tropical circulation. *Quart. J. Roy. Meteor. Soc.,* **106,** 447–462.

Gordon, C. T., and W. F. Stern, 1982: A description of the GFDL global spectral model. *Mon. Wea. Rev.,* **110,** 625–644.

Hoerling, M. P., and A. Kumar, 2003: The perfect ocean for drought. *Science,* **299,** 691–694.

——, J. W. Hurrell, and T. Xu, 2001a: Tropical origins for recent North Atlantic climate change. *Science,* **292,** 90–92.

——, J. S. Whitaker, A. Kumar, and W. Wang, 2001b: The midlatitude warming during 1998–2000. *Geophys. Res. Lett.,* **28,** 755–758.

Hoskins, B. J., I. N. James, and G. H. White, 1983: The shape, propagation and mean-flow interaction of large-scale weather systems. *J. Atmos. Sci.,* **40,** 1595–1612.

Hsiung, J., and R. E. Newell, 1983: The principal nonseasonal modes of variation of global sea surface temperature. *J. Phys. Oceanogr.,* **13,** 1957–1967.

Huffman, G. J., R. F. Adler, A. Chang, R. Ferraro, A. Gruber, A. McNab, B. Rudolf, and U. Schneider, 1997: The Global Precipitation Climatology Project (GPCP) combined precipitation dataset. *Bull. Amer. Meteor. Soc.,* **78,** 5–20.

Kalnay, E., and Coauthors, 1996: The NCEP/NCAR 40-Year Reanalysis Project. *Bull. Amer. Meteor. Soc.,* **77,** 437–471.

Kawamura, R., 1994: A rotated EOF analysis of global sea surface temperature variability with interannual and interdecadal scales. *J. Phys. Oceanogr.,* **24,** 707–715.

Klein, S. A., B. J. Soden, and N.-C. Lau, 1999: Remote sea surface temperature variations during ENSO: Evidence for a tropical atmospheric bridge. *J. Climate,* **12,** 917–932.

Klein, W. H., 1952: The weather and circulation of June 1952: A month with a record heat wave. *Mon. Wea. Rev.,* **80,** 99–104.

Kumar, A., and M. P. Hoerling, 2003: The nature and causes for the delayed atmospheric response to El Niño. *J. Climate,* **16,** 1391–1403.

——, W. Wang, M. P. Hoerling, A. Leetmaa, and M. Ji, 2001: The sustained North American warming of 1997 and 1998. *J. Climate,* **14,** 345–353.

Lanzante, J. R., 1996: Lag relationships involving tropical sea surface temperatures. *J. Climate,* **9,** 2568–2578.

Lau, K. M., and H. Weng, 2002: Recurrent teleconnection patterns linking summertime precipitation variability over East Asia and North America. *J. Meteor. Soc. Japan,* **80,** 1309–1324.

——, K. M. Kim, and J. Y. Lee, 2004: Interannual variability, global teleconnection, and potential predictability associated with the Asian summer monsoon. *East Asian Monsoon,* C.-P. Chang, Ed., World Scientific Series on Meteorology of East Asia, Vol. 2, World Scientific, 153–176.

Lau, N.-C., 1988: Variability of the observed midlatitude storm tracks in relation to the low-frequency changes in the circulation pattern. *J. Atmos. Sci.,* **45,** 2718–2743.

——, and M. J. Nath, 2000: Impact of ENSO on the variability of the Asian–Australian monsoons as simulated in GCM experiments. *J. Climate,* **13,** 4287–4309.

——, and ——, 2003: Atmosphere–ocean variations in the Indo–Pacific sector during ENSO episodes. *J. Climate,* **16,** 3–20.

——, ——, and H. Wang, 2004: Simulations by a GFDL GCM of ENSO-related variability of the coupled atmosphere-ocean system in the East Asian Monsoon region. *East Asian Monsoon,* C.-P. Chang, Ed., World Scientific Series on Meteorology of East Asia, Vol. 2, World Scientific, 271–300.

Manabe, S., R. J. Stouffer, M. J. Spelman, and K. Bryan, 1991: Transient responses of coupled ocean–atmosphere model to gradual changes of atmospheric CO_2. Part I: Annual mean responses. *J. Climate,* **4,** 785–818.

Matsuno, T., 1966: Quasi-geostrophic motions in the equatorial area. *J. Meteor. Soc. Japan,* **44,** 25–43.

Namias, J., 1955: Some meteorological aspects of drought with special reference to the summers of 1952–1954 over the United States. *Mon. Wea. Rev.,* **83,** 199–205.

Pan, Y. H., and A. H. Oort, 1983: Global climate variations connected with sea surface temperature anomalies in the eastern equatorial Pacific Ocean for the 1958–73 period. *Mon. Wea. Rev.,* **111,** 1244–1258.

——, and ——, 1990: Correlation analyses between sea surface temperature anomalies in the eastern equatorial Pacific and the world ocean. *Climate Dyn.,* **4,** 191–205.

Seager, R., N. Harnik, Y. Kushnir, W. Robinson, and J. Miller, 2003: Mechanisms of hemispherically symmetric climate variability. *J. Climate,* **16,** 2960–2978.

Simmons, A. J., and B. J. Hoskins, 1978: The life cycles of some nonlinear baroclinic waves. *J. Atmos. Sci.,* **35,** 1454–1477.

Ting, M., and L. Yu, 1998: Steady response to tropical heating in wavy linear and nonlinear baroclinic models. *J. Atmos. Sci.,* **55,** 3565–3582.

Trenberth, K. E., 1986: An assessment of the impact of transient eddies on the zonal flow during a blocking episode using localized Eliassen–Palm flux diagnostics. *J. Atmos. Sci.,* **43,** 2070–2087.

Wang, B., R. Wu, and X. Fu, 2000: Pacific–East Asian teleconnection: How does ENSO affect East Asian climate? *J. Climate,* **13,** 1517–1536.